Sub-nanometer ceria-promoted Ni 13X zeolite catalyst for CO_2 methanation

Wei, Liangyuan; Grénman, Henrik; Haije, Wim; Kumar, Narendra; Aho, Atte; Eränen, Kari; Wei, Liangfu; de Jong, Wiebren

DOI
10.1016/j.apcata.2021.118012

Publication date
2021

Document Version
Final published version

Published in
Applied Catalysis A: General

Applied Catalysis A, General 612 (2021) 118012

Contents lists available at ScienceDirect

Applied Catalysis A, General

journal homepage: www.elsevier.com/locate/apcata

Sub-nanometer ceria-promoted Ni 13X zeolite catalyst for CO_2 methanation

Liangyuan Wei [a], Henrik Grénman [b,*], Wim Haije [d], Narendra Kumar [b], Atte Aho [b], Kari Eränen [b], Liangfu Wei [c], Wiebren de Jong [a,*]

[a] Faculty 3mE, Department of Process and Energy, Section Large-Scale Energy Storage, Delft University of Technology, Delft, the Netherlands
[b] Faculty of Science and Engineering, Johan Gadolin Process Chemistry Centre, Laboratory of Industrial Chemistry and Reaction Engineering, Åbo Akademi University, Turku/Åbo, Finland
[c] Faculty CiTG, Department of Sanitary Engineering, Delft University of Technology, Delft, the Netherlands
[d] Faculty of Applied Sciences, Department of Chemical Engineering, Section Materials for Energy Conversion and Storage, Delft University of Technology, Delft, the Netherlands

ARTICLE INFO

Keywords:
Sub-nanometer nickel-ceria on zeolite 13X
Citrate complexes
Nickel citrate
Cerium citrate
CO_2 methanation

ABSTRACT

Sub-nanometer zeolite 13X-supported Ni-ceria catalysts were synthesized for CO_2 methanation. XRD and SEM results show the structure and morphology of 13X zeolite after impregnation and calcination. Ce loading affected the catalysts' metal dispersion, reducibility, basicity and acidity, and thence their activity and selectivity. STEM-EDX elemental mappings showed that Ce and Ni are predominantly highly dispersed. Ce has a positive effect on the reduction of NiO and leads to a relatively high number of medium basic sites with a low Ce loading. Highly stable 5%Ni2.5%Ce13X had high activity and nearly 100% CH_4 selectivity in CO_2 methanation at 360 °C, which is mainly due to the high dispersion of metals and relatively high amount of medium basic sites. It can be inferred that this catalyst synthesis strategy has great potential for good catalyst dispersion, since metal uptake by the zeolite is selective for the metal citrate complexes in solution.

1. Introduction

Sorption-enhanced CO_2 methanation has attracted significant attention from researchers in recent years due to its potential in future processes for energy storage and use [1,2]. Water-adsorbing zeolite--supported catalysts were used for the Sabatier reaction [3] ($CO_2 + 4H_2 \leftrightarrow CH_4 + 2H_2O$; $\Delta H^0_{298} = -165$ kJ/mol) in our work to enhance the yield beyond equilibrium according to Le Chatelier's principle and in this way limiting downstream cumbersome separations. When traditional methods are used to prepare catalysts [1,2,4], the dispersion of Ni on zeolite is typically far from single-atom or sub-nanometer. This decreases the activity of the active metal, and increases its inventory. Water-absorption properties of the support have not traditionally been a research focus. Obtaining high metal dispersion on a high capacity water-adsorbing support is a key area of our research. The great potential stems from combining renewable hydrogen (produced with biomass gasification [5], solar and wind power) with CO_2 from stack emissions and eventually Direct Air Capture (DAC), and the distribution and use of renewable methane in the existing infrastructure.

The main challenge in the Sabatier reaction is that rather high temperatures, around 400 °C, are needed for reasonable reaction rates, while thermodynamic conversion is favored at lower temperatures. When the reaction does not proceed to completion, costly separation of the products and reactants is needed, which prohibits the economic viability of the process. There are two ways to tackle this problem: i) developing active catalysts for lower temperatures and ii) removing one of the products, namely water, from the gas mixture to shift the equilibrium to the product side. We seek synergistic effects by using both options, through catalyst-sorbent, *i.e.* bi-functional materials, development. This enables practical application in for example circulating fluidized bed reactors to end up with a continuous process.

Studies on preparing sub-nanometer Ni zeolite catalysts for sorption-enhanced CO_2 methanation are scarce in the literature. Sub-nanometer catalysts are considered ideal catalysts for many reactions, because of the remarkable efficiency of the active metals and excellent activity [6–11]. Few or single-atom based bi-functional materials, *i.e.* having catalytic plus sorption properties, are a promising option (Fig. 1), because they have high activity and should largely retain their water-adsorption capacity by loading only a very limited amount of metal into the support material. Several strategies exist for synthesizing

* Corresponding authors.
E-mail addresses: henrik.grenman@abo.fi (H. Grénman), Wiebren.deJong@tudelft.nl (W. de Jong).

https://doi.org/10.1016/j.apcata.2021.118012
Received 24 September 2020; Received in revised form 9 January 2021; Accepted 11 January 2021
Available online 21 January 2021

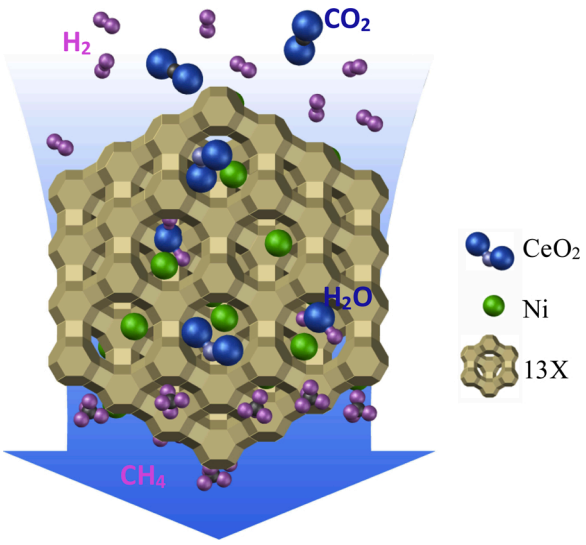

Fig. 1. Schematic representation of sorption-enhanced CO_2 methanation.

sub-nanometer catalysts [10,12], of which mass-selected soft loading [13] and atomic layer deposition [14,15] are limited by high cost and are complicated methods for large-scale catalyst production. In recent years, other synthetic strategies have emerged for single-atom catalyst preparation, such as defect engineering [16,17], coordination pyrolysis [18–20], and gas migration using volatile metal complexes [21]. However, it is difficult to keep the material's structure intact since the high calcination or pyrolysis temperatures will damage the structure of the support irreversibly. Furthermore, there is the possibility of sintering of the metal (nano) particles. Additionally, these preparation routes are difficult to scale up because of the complicated methods involved.

We describe a facile metal-complex precursor strategy to prepare sub-nanometer Ni clusters, or even single-atoms, to be used in combination with the sorbent properties to yield a bi-functional material with great potential for heterogeneous catalysis. A schematic representation of the preparation route is shown in Fig. 2: 13X zeolite was used as the catalyst support as well as the water sorbent for sorption-enhanced CO_2 methanation. Nickel citrate hydrate and cerium nitrate were dissolved in water, where both metal ions compete to form citrate complexes. The size selectivity of the zeolites limits the number of metal complexes that can enter the zeolite and therefore this holds the promise of having very limited Ni and Ce content inside a cage. After calcination, Ni and Ce citrate complexes are decomposed to their respective oxides where CeO_x particles could act as a separator for Ni species in the 13X super cages. We investigated the Ni/Ce ratio effect for Ni:Ce 13X zeolite catalysts with Ce loading varying from 0 to 10 wt.% and Ni loading fixed at 5 wt. % (throughout the paper reference is made to the metal weight percentage). This work focused on the complexation strategy for atomically dispersed Cerium doped Ni-catalyst preparation and characterization. Sorption-enhanced experiments are explicitly not included yet.

2. Experimental section

2.1. Catalyst preparation

The catalysts 5%Ni13X, 5%Ni1%Ce13X, 5%Ni2.5%Ce13X, 5%Ni5%Ce13X and 5%Ni10%Ce13X (metal weight percentages) were prepared by the evaporation impregnation method [22]. A nominal Ni- metal loading of 5% weight was targeted in all 13X zeolite catalysts. Nickel citrate hydrate ($Ni_3(C_6H_5O_7)_2xH_2O$, 98+%, Alfa Aesar) and Ce $(NO_3)_36H_2O$ (Sigma Aldrich, 99.0%) were used as the Ni and Ce precursors. Ni-metal precursors were dissolved in 250 mL of distilled water in a flask, and 5 g of 0.212–0.500 mm size (sieve fraction dried at 100 °C overnight in an oven) 13X zeolite (Honeywell Fluka, The Netherlands) was added to the solution. The 13X zeolite particles used for Ni- and Ce-modification were no longer spherical after treatment in a mortar but had irregular shapes. To prevent mechanical wear of the zeolite particles, the rotary evaporator was operated at low rotation speed, 10 rpm, for 24 h at room temperature. Subsequently the aqueous solution was evaporated in the same at 50 °C using a water jet pump to reduce the pressure. The catalyst was then dried at 100 °C overnight before calcination.

All catalysts were calcined in air in a muffle furnace using a stepwise calcination procedure in air. In the stepwise procedure, the heating rate from room temperature to 250 °C was 4.5 °C/min and the temperature was kept there for 40 min; then it was increased to the target temperature 400 °C by 2.5 °C/min, and kept there for 3 h, then cooled to room temperature.

2.2. Catalyst characterization

The calcined catalysts (before reduction) were characterized by X-ray powder diffraction (XRD), scanning electron microscopy (SEM) with energy-dispersive X-ray spectroscopy (EDX), transmission electron microscopy (TEM), scanning transmission electron microscopy equipped with energy-dispersive X-ray spectroscopy (STEM-EDX), X-ray photoelectron spectroscopy (XPS), hydrogen-temperature programmed reduction (H_2-TPR), Fourier transform infrared (FT-IR), CO_2-temperature programmed desorption (CO_2-TPD), and pyridine-FTIR. Additionally, the reduced catalysts were characterized by N_2 adsorption at 77 K.

A Bruker D8 advance diffractometer and Lynxeye position sensitive detector were used in the XRD measurements. The diffractometer was operated in Bragg-Brentano diffraction mode, and the Cu-*K*α radiation was generated with a voltage of 45 kV and a current of 40 mA. The scanning 2θ angle range in 0D mode was 10.0° to 100.0° using a step size of 0.026°, counting time 2 s/step. The measured XRD diffractograms

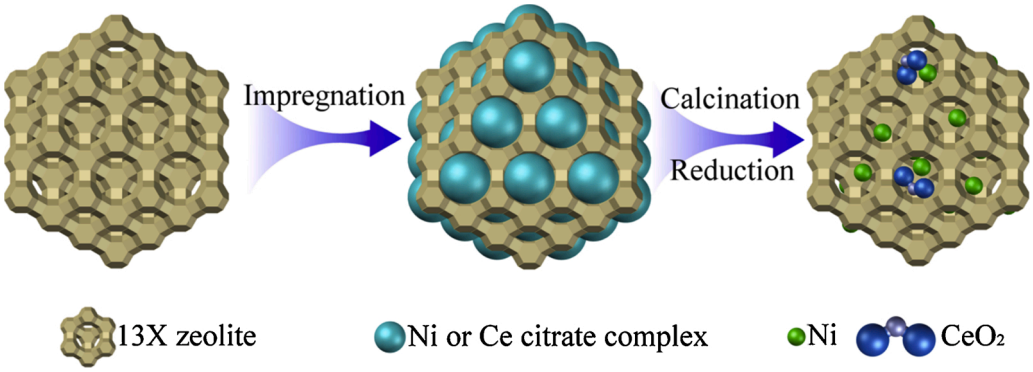

Fig. 2. Schematic representation of catalyst synthesis.

were analyzed with Bruker software DiffracSuite EVA vs 5.0.

Catalyst morphology, shape, size and crystallite distribution were studied by scanning electron microscopy (SEM) JEOL JSM 6500 F (JEOL Ltd., Japan). The imaging modes used were secondary electron imaging (SEI) and back-scattered electron imaging (BEI). Energy dispersive spectroscopy (EDS) was performed with a Thermo Fisher-Noran Ultra-dry silicon drift detector (SDD) and operated and analyzed with the Noran System Seven (NSS) ™ software package (version 2.3).

Transmission electron microscopy (TEM) was used to study the Ni- and Ce-particle size and distribution. The equipment used was JEM-1400 (JEOL Ltd, Japan) with a maximum acceleration voltage of 120 kV.

To further study the nanoscale of catalysts, scanning transmission electron microscopy (STEM) equipped with an energy-dispersive X-ray spectroscopy (EDX) detector was used. The equipment used was FEI Titan 80–300 electron microscope. Elemental mapping was investigated at 300 kV with EDX. Specimen preparation consisted of immersing a lacey carbon film supported on a copper grid into the catalyst powder and small particles adhering to the carbon film were measured.

Determining the dispersion of the nanoparticles was also attempted by H_2 chemisorption with a Micromeritics AutoChem2910. A ratio of H_2: Ni = 1:1 was used in the calculations. Prior to the measurement, the sample was reduced under hydrogen flow at 450 °C after which, the pulsed chemisorption was performed under 5% H_2 in Ar at ambient temperature.

The chemical states of Ce-promoted Ni 13X catalysts were determined using X-ray photoelectron spectroscopy (XPS). A Perkin-Elmer PHI 5400 spectrometer with an Mg Kα X-ray source operated at 14 kV and 200 W was used in the XPS analysis of the samples. The pass energy of the analyzer was 35.5 eV and the energy step 0.1 eV. Peak fitting was performed with the program XPS Peak 4.1. The background was corrected with the Shirley function. Charge compensation was done with the Si 2p peak of the support. A pure 5 wt% Ni13X sample was used as a reference.

H_2-TPR analysis was carried out in a Micromeritics AutoChem 2910. Catalysts were dried at 250 °C for 1 h in a dry Ar atmosphere, then reduced by 5% H_2 diluted in Ar from room temperature to 900 °C with 5 °C/min heating rate. A TCD detector was used to monitor the H_2 consumption.

Fourier transform infrared (FTIR) analysis was performed to investigate the metal complexes in solutions during catalyst preparation. The equipment was a Thermo Scientific Nicolet iS50 FTIR spectrometer with an attenuated total reflectance (ATR) accessory.

CO_2-TPD was performed in a Micromeritics AutoChem II 2920 to investigate the catalyst basic sites. Catalysts were reduced in situ at 450 °C for 2 h with 10% H_2 diluted in Ar, before CO_2 adsorption (10% CO_2 in He) at 50 °C for 1 h. After waiting 30 min for a stable baseline, the CO_2-TPD experiment was carried out from 50 to 750 °C with a heating rate of 10 °C/min under a 50 mL/min He flow.

A pyridine (Sigma-Aldrich, >99.5%) adsorption/desorption study with FTIR was used to investigate the Brønsted or Lewis acid sites of catalysts. An ATI Mattson instrument was used with molar extinction coefficients from Emeis [23].

The surface area and pore volume of fresh 13X, reduced Ni-modified and Ce-promoted Ni zeolite 13X catalysts were measured using nitrogen adsorption. The instrument used was a Micromeritics TriStar II 3020. The fresh 13X and catalysts were outgassed at 350 °C overnight, prior to the surface area measurement. The t-plot analysis was used to get the absorbed volume and specific micro and external surface area (Table S. 8 and Fig. S. 4, supplementary material).

2.3. Evaluation of catalytic properties for the methanation reaction in a fixed-bed reactor

The catalyst activity, selectivity and stability were tested in a quartz fixed-bed reactor with an inner diameter 10 mm. The reactor was filled with silica beads (diameter around 2 mm, around 10 mL) to support the catalyst bed. The silica beads and catalyst were layered by silica wool, and silica beads (around 10 mL) were used to fill the upper part of the reactor (around 12 mm high). The reactor was heated by a vertical tube furnace equipped with a K-type thermocouple, while the temperature of the catalyst bed was monitored by another K-type thermocouple inserted into the bottom of the catalyst bed and connected to a computer. A schematic representation of the fixed-bed reactor system can be found in Fig. S. 1 (supplementary material).

Before the testing, around 0.9 g of calcined catalyst was loaded in the reactor and reduced under 100 mL/min H_2 at 500 °C for 4 h. It was shown that the catalysts reduced at 500 °C had better performance on CO_2 methanation (Fig. S. 2, supplementary material). Catalyst activity experiments were carried out at 240 °C–400 °C with a gas hourly space velocity of around 13,333 mL/$g_{cat.}$/h, in a reaction mixture of 40 mL/min H_2 and 10 mL/min CO_2 diluted in N_2 (150 mL/min). The gas produced from the reactor went through a cooling condenser and was analyzed by GC (Varian, CP-4900 Micro-GC) equipped with HayeSep A, molecular sieve columns (Molsieve 5 Å PLOT) and a thermal conductivity detector. Helium was used as the carrier gas.

The CO_2 conversion (1) and catalyst selectivity (2) for CH_4 are defined as [24,25]:

$$X_{CO_2} = \frac{n_{CO_{2,in}} - n_{CO_{2,out}}}{n_{CO_{2,in}}} \quad (1)$$

$$S_{CH_4} = \frac{n_{CH_{4,out}}}{n_{CO_{2,in}} - n_{CO_{2,out}}} \quad (2)$$

Where $n_{CO_{2,in}}$ is the input molar flow rate of CO_2 in the experiment, $n_{CO_{2,out}}$ and $n_{CH_{4,out}}$ are the molar flow rate of CO_2 and CH_4 calculated from GC results respectively (selectivity <100% means CO is formed).

3. Results and discussion

3.1. Catalyst structure and surface properties

3.1.1. X-ray powder diffraction (XRD)

The XRD results for Ce-promoted Ni 13X catalysts are presented in Fig. 3. The XRD patterns showed no visible peaks for NiO and CeO_2 for any of the samples, which we attribute to the size of NiO particles in the Ni 13X catalysts being too small, < 3 nm, and most probably not well crystallized at the low calcination temperature, leading to significant peak broadening [26]. Similar reasoning applies to CeO_2: the CeO_2 peaks could not be identified even for the 5%Ni10%Ce13×. Small particles are due to the synthesis in which the citrate chelated form of Ni

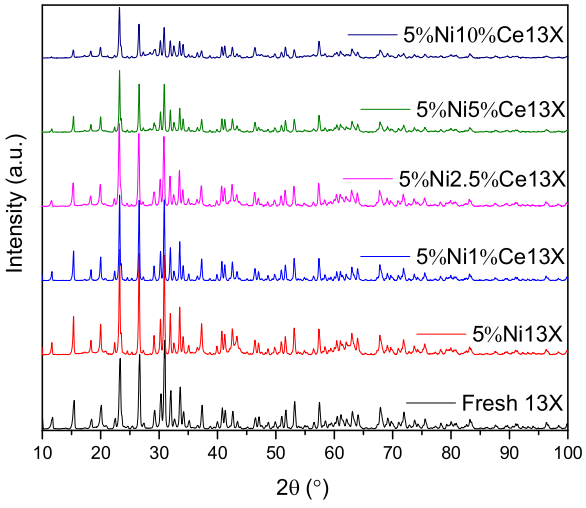

Fig. 3. The XRD patterns for calcined fresh 13X, 5%Ni13X, 5%Ni1%Ce13X, 5% Ni2.5%Ce13X, 5%Ni5%Ce13X and 5%Ni10%Ce13X catalysts.

and Ce were the precursor species in solution. This procedure has been shown to produce small well dispersed particles [27]. The XRD patterns indicated that the crystal structure of 13X zeolite had not changed after the Ni/Ce impregnation using citrate as a complexing agent and calcination treatment. The fresh 13X zeolite patterns were similar to those of the calcined 5%Ni10%Ce13X, 5%Ni5%Ce13X, 5%Ni2,5%Ce13X, 5% Ni1%Ce13X, 5%Ni13X catalysts (Fig. 3).

3.1.2. Scanning electron microscopy (SEM)

The scanning electron micrographs (Fig. 4) showed that the fresh 13X, Ni-modified and Ce-promoted Ni zeolite 13X catalysts were composed of the characteristic fibrous crystals. It was inferred from the morphological studies that the Ni- and Ce-promoted complex strategy did not change the zeolite 13X fibrous morphology. This is in accordance with XRD where no obvious change in crystal habitus was observed, induced by a change in preferred orientation. On the other hand, according to the EDX results (Table S. 2, supplementary material), the Al and Si ratios as well as the charge neutralizing cations' quantities in the modified catalysts, were close to fresh 13X zeolite, which again showed that the 13X zeolite composition did not significantly change after Ni (Ce) modification procedures.

3.1.3. Transmission electron microscopy (TEM)

TEM was used to investigate the NiO and CeO_2 particle size distribution. The TEM images of the Ce-promoted Ni catalysts are shown in Fig. 5. Nano particles are observed in all impregnated samples. The ones in the 5 and 10% Ce are clearly much bigger (tens of nm) than the highly dispersed ones in the 1 and 2,5% Ce samples, which are of the order of 1 nm. The characteristic 13X channels can be clearly seen. Indeed, some NiO clusters could be observed in 5%Ni13X, in which a possible dispersion effect of Ce did not occur. However, the larger particles were observed in the catalysts with higher Ce loading (5%Ni5%Ce13X and 5% Ni10%Ce13X). The possible explanation here is that Ce promoted the Ni dispersion during the catalyst preparation, but the excess Ce formed 3D clusters when the Ce loading was higher than 5 wt.% mostly outside the zeolite confinement. The characterization of the textural properties of the 13X zeolite as fresh, 5%Ni13X, 5%Ni1%Ce13X, 5%Ni2.5%Ce13X, 5%Ni5%Ce13X, 5%Ni10%Ce13X catalysts using transmission electron microscopy clearly showed the characteristic fibrous structure, as well as the ordered uniform pores and channel systems (Fig. 5).

Due to limitations of the TEM used we cannot distinguish between Ce or Ni containing particles. That is why elemental mapping was used in Fig. 6. In Fig. 5 it is clear that pristine zeolite does not contain particles and samples where Ni is diluted with Ce show the best dispersed, small, particles, as substantiated in the mappings (Fig. 6).

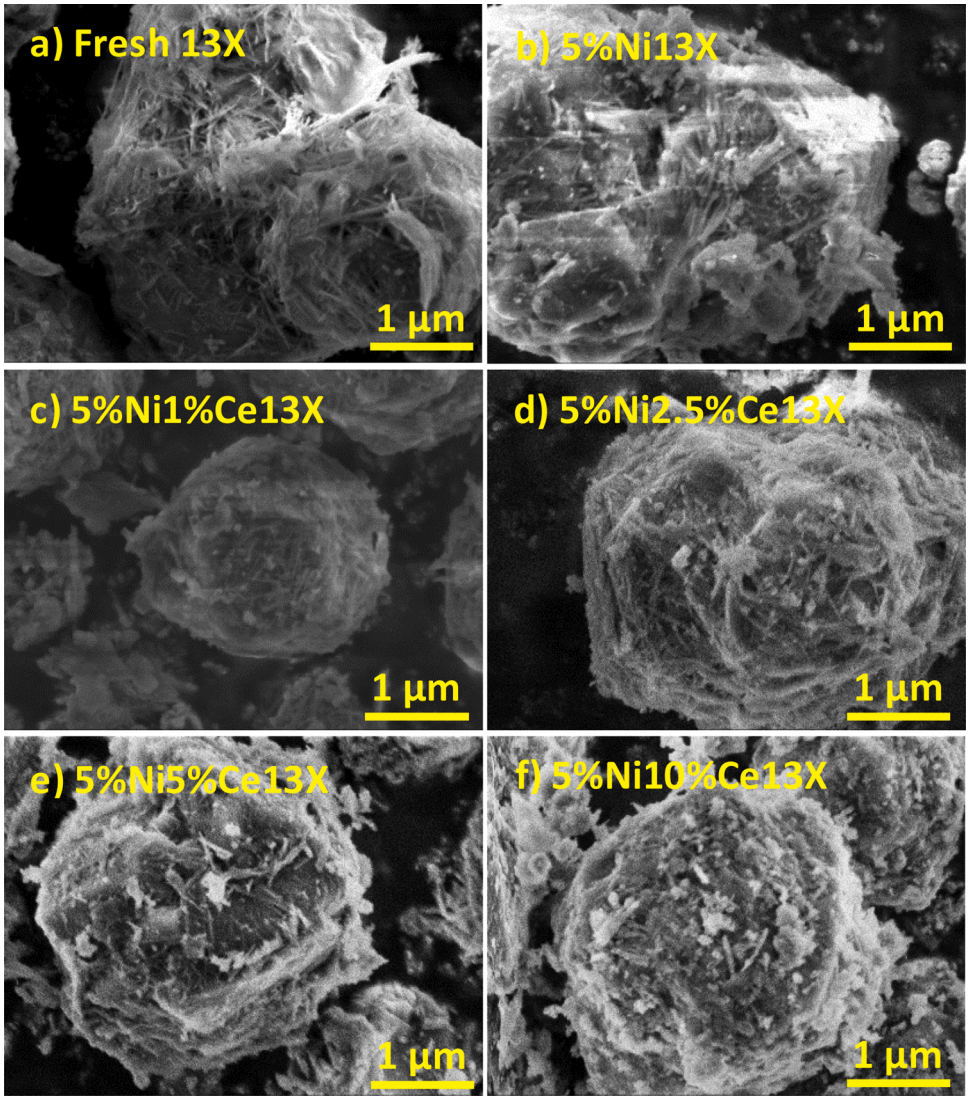

Fig. 4. SEM images of a) fresh 13X, b) 5%Ni13X, c) 5%Ni1%Ce13X, d) 5%Ni2.5%Ce13X, e) 5%Ni5%Ce13X and f) 5%Ni10%Ce13X catalyst.

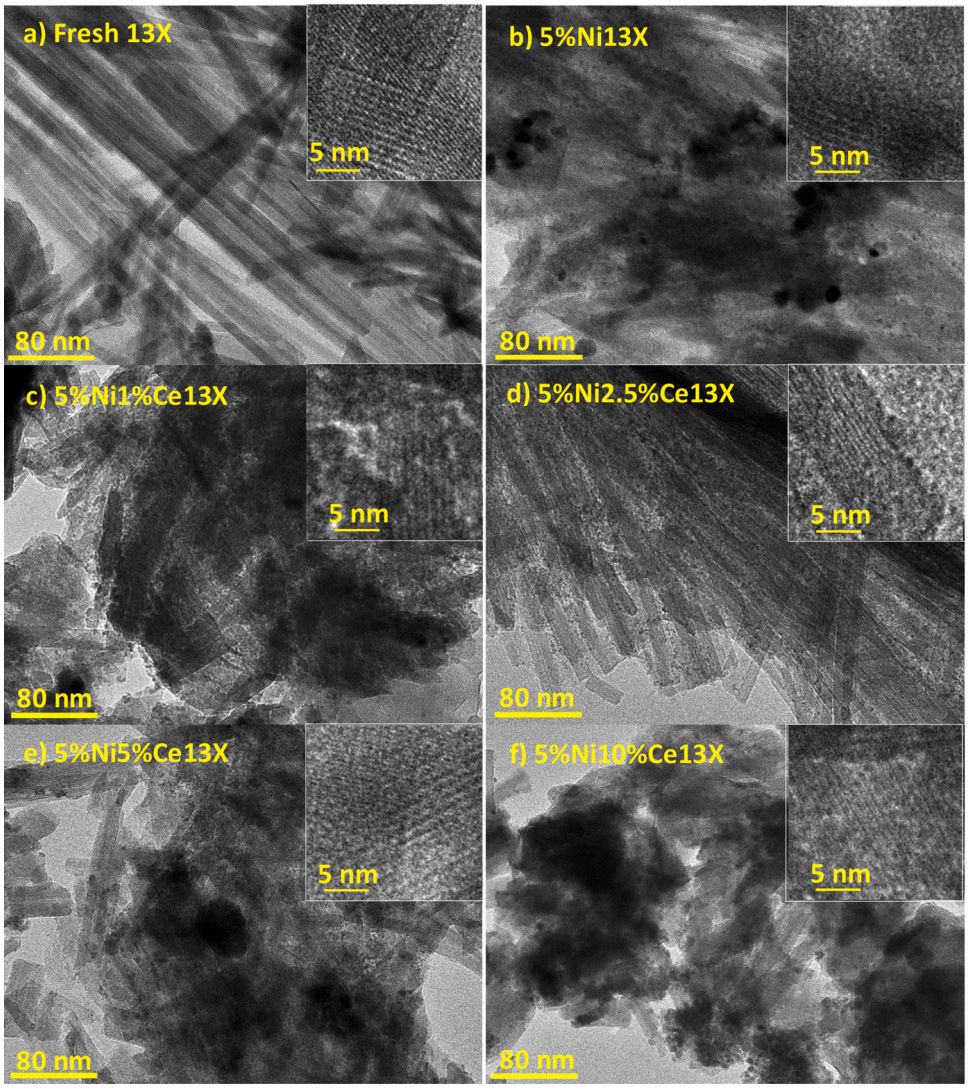

Fig. 5. TEM images of a) fresh 13X, b) 5%Ni13X, c) 5%Ni1%Ce13X, d) 5%Ni2.5%Ce13X, e) 5%Ni5%Ce13X and f) 5%Ni10%Ce13X catalyst.

3.1.4. Elemental mapping

A closer study of the dispersion of Ni and Ce on or in the 13X zeolite, and the determination of the relative distribution of Ni and Ce, was carried out through an elemental mapping with STEM-EDX (Fig. 6). Ni is dispersed well on both 5%Ni2.5%Ce13X and 5%Ni13X, and the Ce also shows a good dispersion on 5%Ni2.5%Ce13×.

In Fig. 6 (20 nm and 5 nm scale bar) we see that Ni and Ce are highly dispersed and may be present even as single atoms in 5%Ni2.5%Ce13×. Since the diameter of 13X zeolite pores is around 7.4 Å [28], while CeO_2 is between 5.5–7.5 Å, and NiO is around 3.24 Å [29], it is hardly possible for more than one or a pair of NiO and/or CeO_2 to co-exist in a zeolite super-cage. Additionally, it is obvious that the Ni and Ce are overlapping in 5%Ni2.5%Ce13X The lowest row in Fig. 6 clearly shows the high dispersion of both Ce and Ni in very small sub-nanometer cluster size. This implies that Ni atoms in the reduced state are isolated by surrounding Ceria, if space permits, or are just on their own. This substantiates the close proximity of Ni and Ce.

Determining the dispersion of the nanoparticles was also attempted by H_2 chemisorption, however, the method gave unrealistically low values for the dispersion indicating an average metal particle size of tens of micrometers. The adsorbed volume of hydrogen on the catalyst 5% Ni2.5%Ce13X was 0.04354 mL/g_cat, which corresponds to 1.94 µmol/g_cat (Fig. S.5 in supporting material). The nominal loading of nickel on the catalyst, on the other hand, was 851.9 µmol/g_cat, which would indicate very low dispersion. The verified chemisorption result shows that the method is not suitable for measuring metal dispersion of these catalysts, as TEM and STEM images taken from multiple locations of each catalyst show very small particle sizes. This lead to the conclusion that direct visual observation with TEM and STEM is more suitable for these catalysts.

3.1.5. H_2-Temperature programmed reduction (H_2-TPR)

The H_2-TPR profiles of Ni- and Ce-promoted Ni 13X catalysts are shown in Fig. 7. Two major peaks were observed for all catalysts. It has been reported that the first reduction peak corresponds to NiO particles outside the zeolite or in super-cages and the second peak to NiO particles in sodalite cages [30,31]. It is noticeable that the intensity of the TCD signal in the second peak became weaker with increased loading of Ce, and that the ratio of the first peak to the second peak increased with increasing Ce loading, which might indicate that less NiO appeared in sodalite cages. Efforts to quantify the hydrogen amount consumed in the reduction led to values in excess of the theoretical amount of NiO present in the samples. Table 1 displays the amount of catalyst analyzed (m_cat (g)), the amounts of Ni and Ce, the consumed amount of hydrogen as well as the ratio of consumed hydrogen and the amount of nickel (n_H_2/n_Ni). As can be seen from the values, the amount of consumed hydrogen exceeds the theoretical amount of Ni present in the samples and the ratio increases with increasing ceria content. This is

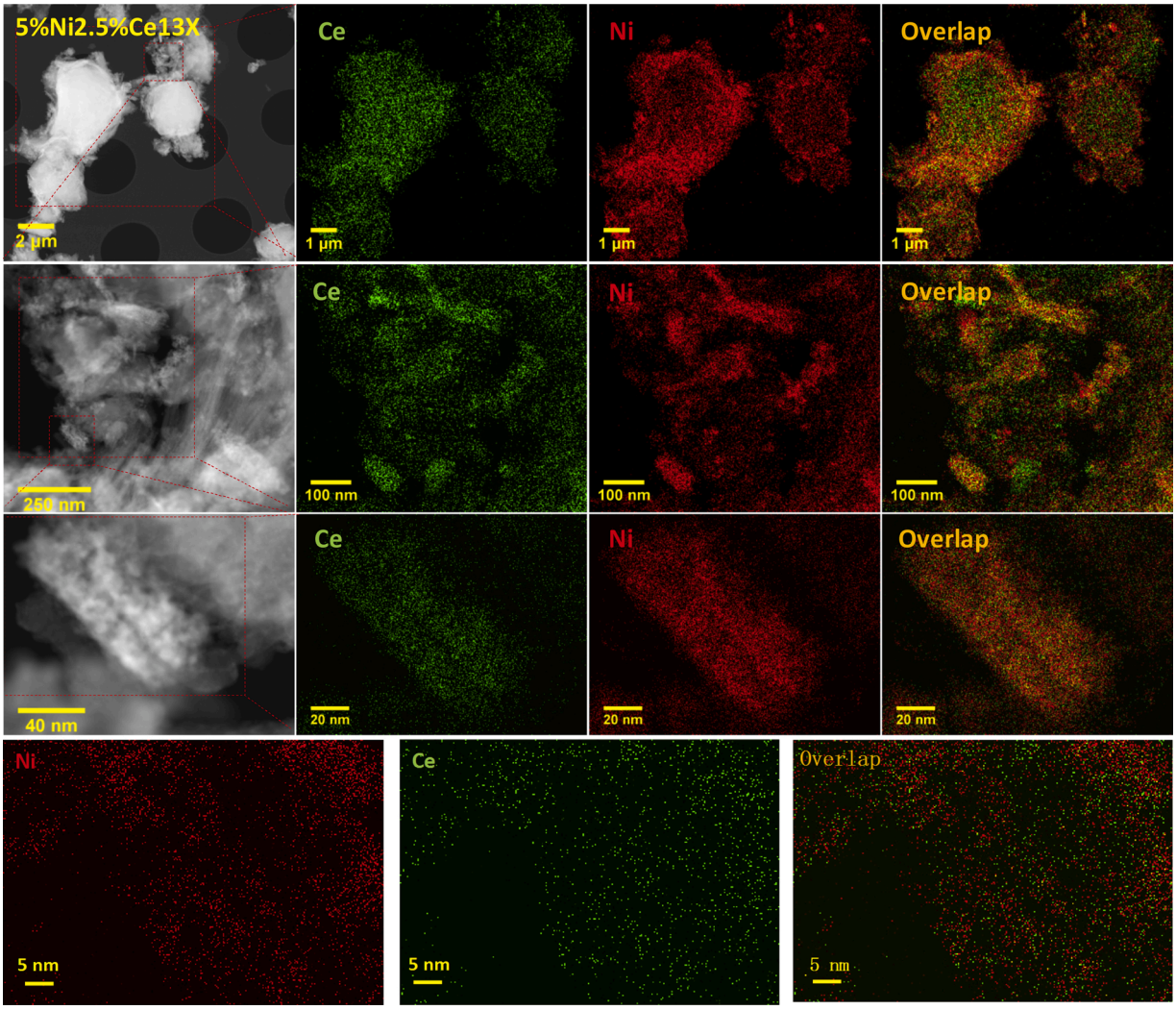

Fig. 6. STEM images Ni (red), Ce (green) and Ce Ni overlap (yellow) maps of 5%Ni2.5%Ce13X at four magnifications.

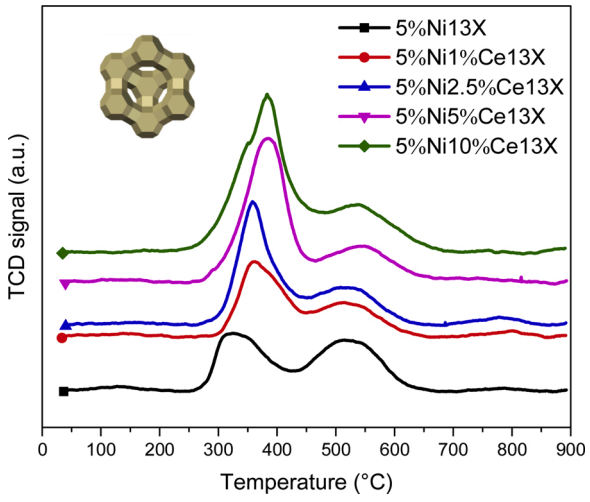

Fig. 7. H_2-TPR profiles of 5%Ni13X, 5%Ni1%Ce13X, 5%Ni2.5%Ce13X, 5% Ni5%Ce13X and 5%Ni10%Ce13X catalysts (same scale for all traces).

most probably a result of both spill-over from the Ni to the support as well as reduction of the ceria [32].

The first reduction peak of Ce-promoted Ni 13X catalysts became stronger with increasing Ce loading. This may result from the improved dispersion of Ni species [33] and the partial reduction of CeO_2 [34]. Additionally, the two reduction peaks of the catalyst were shifted slightly to a higher temperature upon increasing Ce loading. For 5% Ni13X, the first peak appeared at around 325 °C and a second reduction peak at around 545 °C. After the Ce loading, the first reduction peak shifted to around 360 °C for 5%Ni1%Ce13X, even to 380 °C for 5% Ni10%Ce13 × . It has been reported that the reduction peaks of Ce-promoted Ni/γ-Al_2O_3 catalysts shifted to a lower temperature, since the Ce^{4+}/Ce^{3+} redox couple created surface and bulk oxygen vacancies [35]. This could be due to the CeO_2 which on the surface or in super-cages of 13X limited the H_2 reaching NiO, due to the size of CeO_2 [29] (5.5–7.5 Å) and pore size of 13X (7.4 Å) [28]. The highly dispersed sub-nanometer sized NiO and CeO_2 clearly results from the size exclusion of 13X zeolite for Ni and Ce citrate complexes during catalyst preparation.

In relation to the seemingly deviating trend of the 5%Ni5%Ce13X the following can be argued. The general trend is a shift to higher T for both distinct peaks (in fact envelopes). The samples are quite inhomogeneous in nature so it is not clear if the Ni/Ce ratio inside and outside the particles is always the same and that will certainly give rise to different reduction behavior. Furthermore, the accuracy of the temperature inside the sample can cause the observed, seemingly, deviating behavior.

Table 1
Temperature programmed reduction of the catalysts.

Catalyst	m_cat (g)	Ni %	Ce %	n_Ni (mmol)	n_Ce (mmol)	V_H_2 (ml)	n_H_2 (mmol)	n_H_2/n_Ni
5%Ni13X	0.2013	5.00	0.00	0.1715	0.0000	16.89	0.6905	4.03
5%Ni1%Ce13X	0.1934	5.00	1.00	0.1648	0.0138	19.41	0.7935	4.82
5%Ni2.5%Ce13X	0.1977	5.00	2.50	0.1684	0.0353	18.05	0.7379	4.38
5%Ni5%Ce13X	0.2071	5.00	5.00	0.1764	0.0739	24.14	0.9869	5.59
5%Ni10%Ce13X	0.1893	5.00	10.00	0.1613	0.1351	31.43	1.2849	7.97

3.1.6. Fourier transform infrared spectrometry

ATR-FTIR was used to investigate the Ni and Ce complexes during catalyst preparation, to determine the coordination shell of the metals in solution, which may determine how metals disperse in catalysts. The FTIR spectra of the solutions are shown in Fig. 8, and Table S. 3 (supplementary material) shows the adsorption band assignments. Citric acid, nickel nitrate, cerium nitrate and nickel citrate mixed with nickel nitrate solution were the references.

Overall, the ATR-FTIR spectra of solutions e, f and i are much different to free Ce solutions (Fig. 8). For nickel citrate mixed with cerium nitrate solution, the bands at 1607 cm^{-1} disappeared and a strong band was observed at 1542 cm^{-1}. These two ν_{as} carboxylate stretch-associated bands' changes may result from the new complex (e.g. $[Ce(HCit)(Cit)]^{2-}$), which has a longer bond length than $[Ni(HCit)(Cit)]^{3-}$, eventually leading to the band shifting to a lower wavenumber and 1607 cm^{-1} disappearing [36–38]. The band at 1434 cm^{-1} is also more obviously visible than free cerium solutions, and two new bands at 1298 and 1265 cm^{-1} were observed for citric acid mixed with nickel nitrate solution and nickel citrate mixed with cerium nitrate solution. Other right-shift bands are found at 1249, 1178 and 1141 cm^{-1} for cerium solutions. These differences could be contributed by the ν_s carboxylate stretch in the Ce citrate complexes [36,37,39]. In summary, the FTIR spectra show that Cerium ions also complexate with citrate in competition the nickel citrate complexes. The competition is shown to prove that both Ce and Ni are available to the zeolite as citrate complexes, thereby excluding large amounts to penetrate the pores because of the complex' size. This adds to the final conclusion of the presence of very small Ni-Ce clusters, if not even 'single-atom' ones.

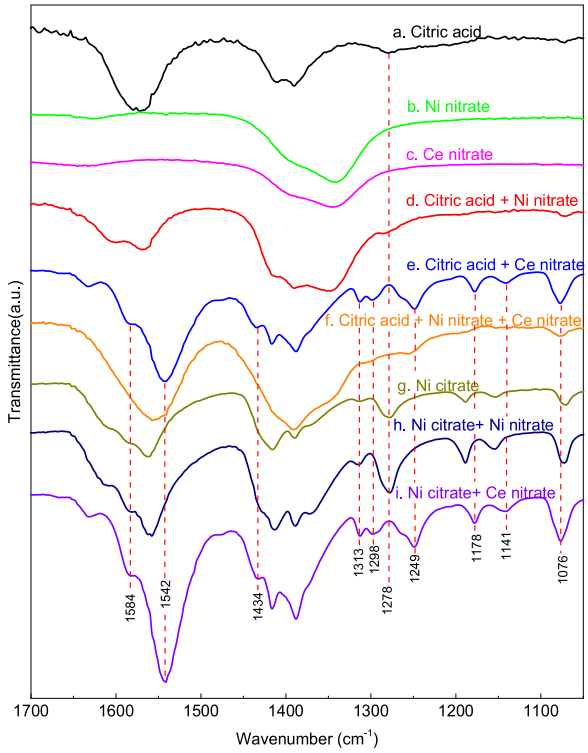

Fig. 8. ATR-FTIR spectra for aqueous solutions: a) citric acid, b) nickel nitrate, c) cerium nitrate, d) citric acid mixed with nickel nitrate, e) citric acid mixed with cerium nitrate, f) citric acid mixed with nickel nitrate and cerium nitrate, g) nickel citrate, h) nickel citrate mixed with nickel nitrate and i) nickel citrate mixed cerium nitrate. Solutions d, e and f were prepared with stoichiometric ratios. In solution f the molar ratio of Ni:Ce is 1:1, in solution h the molar ratio of nickel citrate to nickel nitrate was 0.83, and in solution i the molar ratio of nickel citrate to cerium nitrate was 0.83. The pH of solutions a, d, e and f were adjusted using 3.4 M KOH solution to around 4.5.

3.1.7. X-ray photoelectron spectroscopy (XPS)

The chemical valence states of the Ni and Ce in samples were investigated using X-ray photoelectron spectroscopy (Fig. 9 and supplementary Fig. S. 3). In Fig. 9b, a peak observed in the Ni $2p_{3/2}$ at 856.1 eV is assigned to Ni^{2+}; it was accompanied by satellite peaks at around 861.6 eV [40]. Because the $NiSiO_3$ and $NiAl_2O_4$ peaks are at 856.1 eV and 855.8 eV, respectively, this indicates that the Ni particles interacted strongly with zeolite 13X via Ni-O-Si(Al) bonding [41]. It could be inferred that the Ni particles in 5%Ni5%Ce13X show similar behavior to 5%Ni2.5%Ce13X, due to their closely resembling spectra (Fig. 9b and d). The XPS spectra of Ce 3d (Fig. 9a and c) were fitted to several peaks corresponding to Ce $3d_{5/2}$ (v, 898.0 eV) and Ce $3d_{3/2}$ (u_0, 898.7 eV; u, 901.3 eV; u_1, 902.2 eV; u_2, 908.2 eV; u_3, 916.7 eV). The u_0 and u_3 are attributed to Ce^{3+} species, and the remaining peaks (v, u, u_1, u_2) are Ce^{4+} species [42].

The X-ray photoelectron spectroscopy of the 5 wt.% Ni-13X catalyst has been included for reference in Fig. 9e and f. Taking into consideration that the catalyst is monometallic i.e, Ni modified 13X zeolite without Ce, XPS spectra did not exhibit the presence of Ce^{3+} or Ce^{4+} peaks at binding energies 890−920 eV. The peaks attributed to Ni^{2+} (856.1 eV) and a satellite peak (861.6 eV) were observed at binding energies 840−890 eV.

Clearly, since u_0 and u_3 indicate Ce^{3+}, v, u, $u_{,1}$ and u_2 indicate Ce^{4+} species, in Fig. 9a, the 5%Ce-5%Ni sample, only u as indication of Ce^{4+} is visible, whereas in Fig. 9c, the 2,5%Ce-5%Ni sample, c, v, u, u_1 and u_2 are clearly visible. U_0 and u_3 are similarly visible in both samples, therefore there is more Ce^{4+} in low loadings of Ce.

3.1.8. CO_2-temperature programmed desorption (CO_2-TPD)

Fig. 10 shows the CO_2-TPD profiles of fresh 13X and modified catalysts. The calculated basic site distribution is shown in Fig. 11 (for detailed information, see supplementary material Table S. 5). Most of the samples have three peaks at around 50–150 °C, 250–450 °C and 450–750 °C, which generally correspond to weak, medium and strong basic sites, respectively [43]. These three basic sites are assigned to surface hydroxyl groups, metal-oxygen pairs and low-coordination oxygen anions, respectively [44]. Mass Spectroscopy installed downstream of a cold trap to remove the water, clearly showed that only the first peak of the TPD experiment is related to CO_2 evolution, the others to water desorption and decomposition, respectively. Overall, the fresh 13X has the most basic sites. The reason for formation of basic sites is the chemical composition of 13X zeolite (Table S. 2). The presence of large amounts of basic sites can be attributed to the presence of alkaline metal oxides: Na (11.2 wt.%), Mg (1.3 wt.%), Ca (0.3 wt.%), K (0.3 wt.%) in

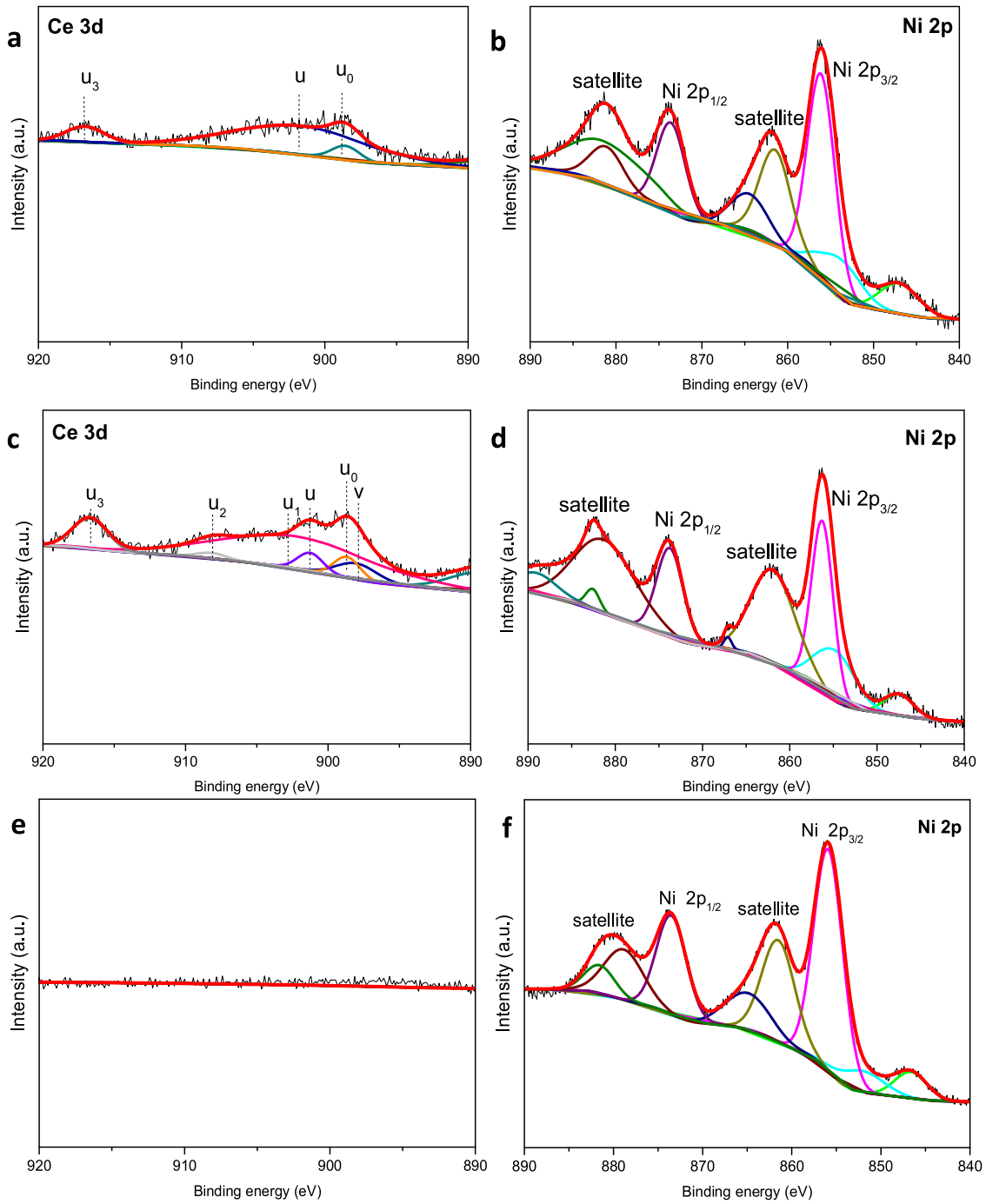

Fig. 9. (a) Ce 3d XPS spectra in 5%Ni2.5%Ce13X; (b) Ni 2p XPS spectra in 5%Ni2.5%Ce13X; (c) Ce 3d XPS spectra in 5%Ni5%Ce13X; (d) Ni 2p XPS spectra in 5% Ni5%Ce13X ; (e) Ce 3d spectra in 5%Ni13×., (f) Ni 2p XPS spectra in 5%Ni13×.

the fresh 13X zeolite (Table S. 2). The largest amount of total basic sites among the impregnated catalysts was obtained for 5%Ni10%Ce13X (Fig. 11).

The basicity decreased significantly after modification, which can only partly be attributed to the removal of Na, Ca, K, Mg from 13X zeolite by ion exchange. Compared to 5%Ni13X, with only nickel, the basicity decreased when Ce was increased up to loading of 2.5 wt.%. When the Ce loading was further increased, the total basicity increased again. It has been reported that Ce^{3+} can act as Lewis base adsorbing CO_2 [45,46]. A reasonable explanation could be that at low Ce loadings the Ce^{4+} is the dominant charge in the smaller Ni/Ce particles, whereas bulkier particles that are also mainly outside the zeolitic framework contain more Ce^{3+}, causing an increase in basicity again [47].

Furthermore, the basicity of 5%Ni2.5%Ce13X was very similar to 5% Ni2.5%Ce13X-3 h, which was reduced in situ for 3 h at 450 °C instead of 2 h. This shows that the basicity of catalysts is stable after 2 h of reduction before the catalyst test experiments.

3.1.9. Measurement of Brønsted and Lewis acid sites by FTIR using pyridine as probe molecule

The concentration of Brønsted acid sites (BAS) and Lewis acid sites (LAS) in the pristine and titrated zeolites was determined with FTIR using pyridine as a probe molecule method [23,48–50]. The results are shown in Fig. 12 (for detailed information, see supplementary material

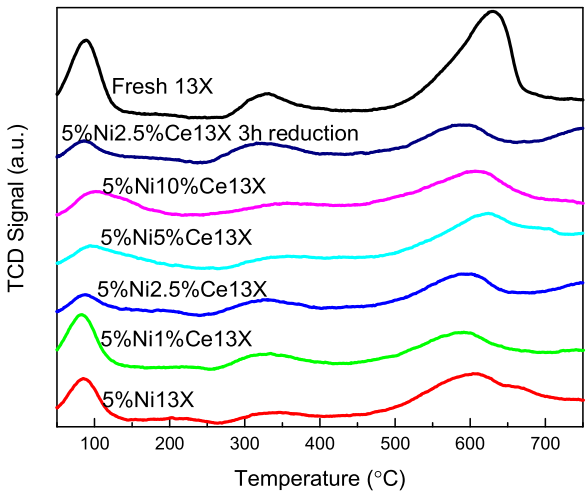

Fig. 10. CO_2-TPD profiles of fresh 13X, 5%Ni13X, 5%Ni1%Ce13X, 5%Ni2.5% Ce13X, 5%Ni5%Ce13X and 5%Ni10%Ce13X catalyst.

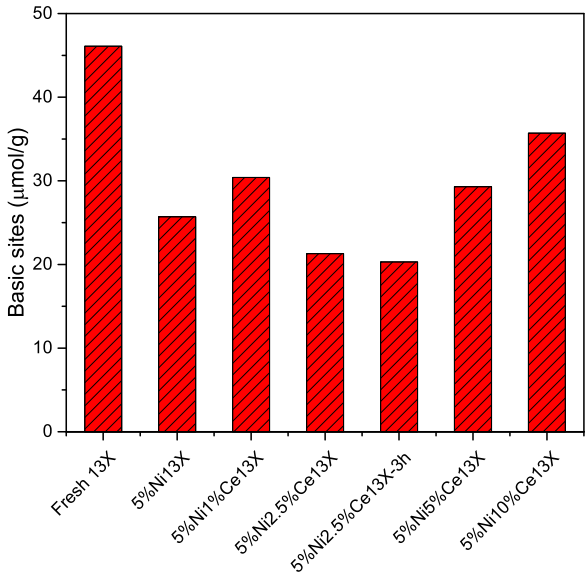

Fig. 11. Catalyst basic site content, calculated based on the results of CO_2-TPD.

Table S. 6).

Overall, compared to fresh 13X, the catalysts' total acidity decreased after the Ni modification promoted by Ce. The lowest total acidity of 427 μmol/g was measured for 5%Ni2.5%Ce13X among 13X catalysts, which is much lower than the other Ce-promoted Ni 13X catalysts. With increasing Ce amount, the acidic sites could be shielded or blocked by the higher Ce loading in the catalysts [50]. It should be noted, however, that Brønsted acid sites and Lewis acid sites in the catalysts changed significantly after the Ce-promoted Ni modification. The Lewis acid sites decreased from 545 μmol/g to 196 μmol/g (250 °C), while the Brønsted acid sites increased dramatically from 12 μmol/g to 282 μmol/g (250 °C), then decreased to 122 μmol/g for 5%Ni2.5%Ce13X, and increased again with increasing Ce loading. This effect is largely due to the low pH = 4.5 of the impregnating solution [27]. It can be concluded that Ni impregnation increased the amount of Brønsted acid sites for 13X zeolite catalysts, where relatively low Ce loading decreases it (Table S. 6, supplementary material). The presence and amount of Brønsted acid sites in the 13X fresh zeolite, Ni- and Ce- modified 13X catalysts can in large part be attributed to the Al species in the tetrahedral coordination. Given the very small variations in the number Al species in the zeolite this cannot

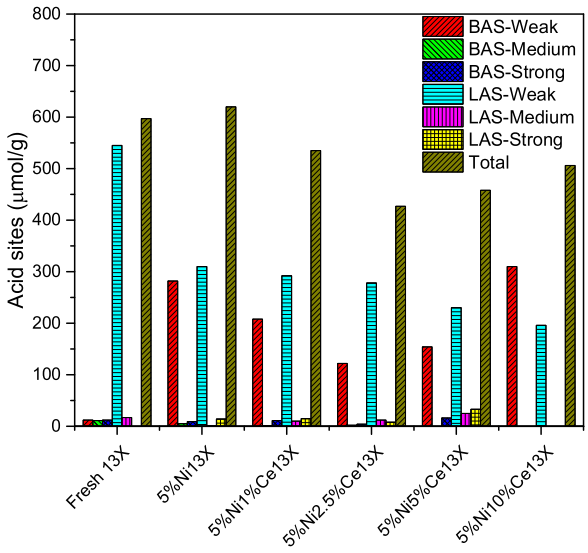

Fig. 12. Concentrations of Brønsted acid sites (BAS) and Lewis acid sites (LAS) determined with the FTIR-pyridine method for fresh 13X, 5%Ni13X, 5%Ni1% Ce13X, 5%Ni2.5%Ce13X, 5%Ni5%Ce13X and 5%Ni10%Ce13 × .

be the whole story.

3.2. Evaluation of catalytic properties in methanation using a fixed-bed reactor

3.2.1. Catalyst activity and selectivity

Catalyst activity and selectivity were investigated on a lab-scale fixed-bed reactor system. Details about experimental conditions and settings are in the experimental section. The results are shown in Fig. 13. A comparison of catalyst performance with literature results can be found in Table S. 7 (supplementary material). The CO_2 conversion at each temperature was the average value based on GC measurements of five consecutive stable measurements, after the zeolite 13X adsorbed water under experimental conditions. The adsorption enhancement can be excluded from the data.

Overall, it can be observed from Fig. 13 that the catalyst around the minima in Fig. 11 and Fig. 12, 5%Ni1%Ce13X, 5%Ni2.5%Ce13X and 5% Ni5%Ce13X, performed best. In other words, neither the acidity nor basicity should be too strong, but a balanced amount of both are needed. Furthermore, Lewis acidity is not as influential as Brønsted acidity and the basic sites should clearly not be too strong [51]. The activation energy is rather high and we observed the largest conversion gain compared with the literature at between 280 and 320 °C (Table S. 7, supplementary material). 5%Ni2.5%Ce13X and 5%Ni1%Ce13X are really highly active catalysts and display the highest reported low temperature (below 300 °C) activity with industrially relevant catalyst particle sizes.

Ce has a significant influence on the catalyst performance for CO_2 conversion. It has been reported that the oxygen vacancy resulting from Ce could contribute to the catalyst activity [45], but in the 5%Ni5% Ce13X and 5%Ni2.5%Ce13X the Ce^{3+}/Ce^{4+} ratios are equal. It must therefore rather be ascribed to the basicity of ceria which is stronger in the 2.5–5% case. Even though both the weak and medium basic sites are beneficial for CO_2 activation [52] and Ce-promoted catalysts have more weak and medium basic sites than 5%Ni13X (Fig. 11), the pores blocked by excess Ce oxides counteract this effect at higher loadings. The theoretical maximum Ce loading is around 3.4 wt.% for the case that Ce only located in 13X super cages, which was calculated based on the crystal structure of 13X zeolite. The catalysts surface area and pore volume can be found from supplementary material (Fig. S. 4 and Table S. 8). Too strong adsorption of CO_2 to the strong sites could also account for the

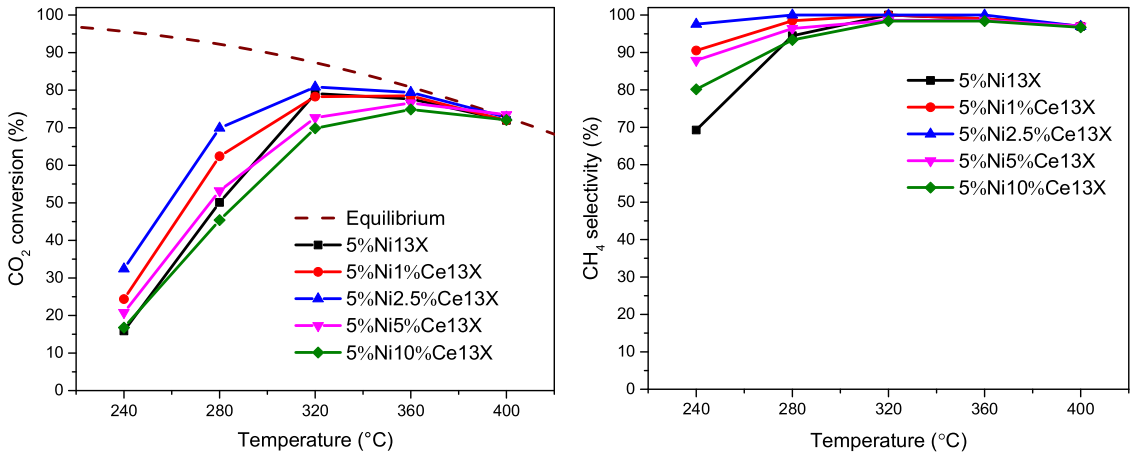

Fig. 13. CO_2 conversion and CH_4 selectivity with 5%Ni13X, 5%Ni1%Ce13X, 5%Ni2.5%Ce13X, 5%Ni5%Ce13X and 5%Ni10%Ce13X catalyst (reduction at 500 °C, 4 h), 0.9 g, 150 mL/min N_2, 40 mL/min H_2, 10 mL/min CO_2.

lower 5%Ni5%Ce13X and 5%Ni10%Ce13X activities.

The role of the acidic sites is explained in the following. CO_2 methanation on Ni is proposed to proceed via dissociative adsorption of hydrogen followed by a reactive adsorption of CO_2 forming a formate intermediate. The formate then reacts with an additional hydrogen to form water and CO. The rate limiting step of the overall reaction is the dissociation of CO to form adsorbed carbon and oxygen intermediates [53]. It is proposed that the acid base balance of the support influences the dissociation of CO on the Ni surface, especially at lower temperatures. This is reflected in the activity of the catalyst as it is the rate limiting step as well as in the selectivity towards CH_4. Higher activity is thus directly correlated with higher selectivity as displayed in Fig. 13. The selectivity is decreased when CO is partly desorbed before it is dissociated.

$$H_2(g) + 2ad \leftrightarrow 2Had \quad (3)$$

$$CO_2(g) + Had \leftrightarrow HCOOad \quad (4)$$

$$HCOOad + Had \leftrightarrow H_2Oad + COad \quad (5)$$

$$COad \leftrightarrow Cad + Oad \text{ (rate limiting step)} \quad (6)$$

In general, all catalysts show good CH_4 selectivities, especially for 5%Ni1%Ce13X and 5%Ni2.5%Ce13X, which show CH_4 selectivity higher than 95% at 280–400 °C. Fig. 13 shows that Ce is not always beneficial to CH_4 selectivity when the Ce loading is higher than 2.5%. This could again be attributed to the influence of Ce on catalysts' basic sites and acidity (Fig. 11, Fig. 12). Pore blockage (Table S. 8, supplementary material) plays a role here as well: the external surface area is similar for all catalysts but the micropore related surface area decreases with increasing Ceria content.

3.2.2. *Catalyst stability and selectivity*

The preliminary catalyst stability test results of 5%Ni2.5%Ce13X and 5%Ni13X are displayed in Fig. 14. The catalyst stability tests were carried out in the lab-scale fixed-bed reactor system at 360 °C for 200 h; other conditions for evaluation of catalytic properties in the methanation reactions were described in the experimental section above.

The conversions are in full agreement with Fig. 13. It can be concluded for the Ce-promoted sub-nanometer Ni clusters 13X catalyst, that no changes in visual appearance, indicating e.g. carboneous deposits, or significant changes in conversion or selectivity in CO_2 methanation were observed at a high temperature for 200 h time-on-stream. The fact that no severe deactivation occurs even at this higher temperature, makes it very unlikely that it would occur at lower temperature. However, a systematic study of the stability and selectivity at different temperature, feed composition and conversion levels should be performed to obtain conclusive results. This is considered to be outside the scope of this contribution.

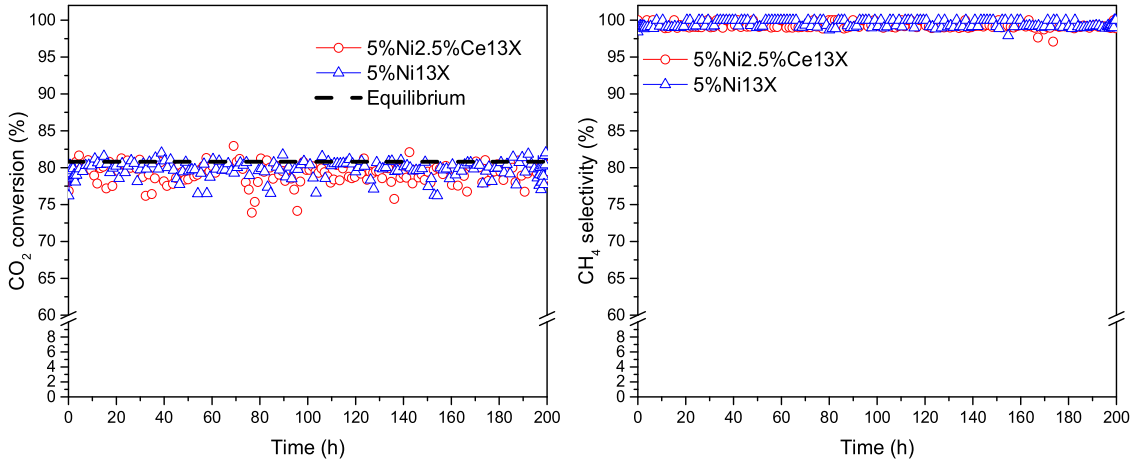

Fig. 14. CO_2 conversion and CH_4 selectivity of 5%Ni2.5%Ce13X and 5%Ni13X at 360 °C (reduction at 500 °C, 4 h), 0.9 g, 150 mL/min N_2, 40 mL/min H_2, 10 mL/min CO_2.

4. Conclusions

Active functional ceria-promoted Ni 13X zeolite catalysts were synthesized using a citrate complexation strategy for CO_2 methanation. The influence of Ce loading on catalyst properties and the catalysts' performance were investigated. The results showed that the loading of Ce affected the catalysts' metal dispersion, reducibility, basicity and acidity, and as a consequence their activity and selectivity. Activity increase is most pronounced at lower temperatures, below 280 °C, selectivity is satisfactory from this temperature upward. XRD and SEM results showed that the structure of 13X zeolite did not change after citrates' impregnation and calcination. TEM and STEM-EDX mappings showed that most Ce and Ni were highly dispersed as sub-nanometer. Ce and Ni ions were chelated by citrate and as such diffused in the zeolite structure. It was shown that there was a strong correlation between acidity, basicity and conversion: neither should be too strong and a balance should prevail. The basicity should not be too high to result in too strong bonding of CO_2 and the acidity should not be too high to allow for interaction with CO_2. The catalysts' stability test results showed that the highly active catalyst 5%Ni2.5%Ce13X had a very stable performance on CO_2 methanation and high CH_4 selectivity for a 200 -h timescale.

In summary, using Ni and Ce citrate complexes is a very promising strategy to prepare highly dispersed sub-nanometer ceria-promoted Ni catalytic particles in zeolite 13X. The metal precursors in solution both exist as citrate complexes and the catalyst supports are selective to these complexes' size and geometry. It can be inferred that this strategy has significant potential for the preparation of highly active sub-nanometer even single-atom catalysts.

CRediT authorship contribution statement

Liangyuan Wei: Conceptualization, Software, Investigation, Formal analysis, Data curation, Visualization, Writing - original draft. **Henrik Grénman:** Conceptualization, Methodology, Resources, Supervision, Project administration, Funding acquisition, Writing - review & editing. **Wim Haije:** Conceptualization, Investigation, Methodology, Supervision, Writing - review & editing. **Narendra Kumar:** Methodology, Investigation, Formal analysis, Resources, Supervision, Writing - review & editing. **Atte Aho:** Investigation. **Kari Eränen:** Investigation. **Liangfu Wei:** Investigation. **Wiebren de Jong:** Resources, Supervision, Writing - review & editing.

Declaration of Competing Interest

The authors declare that they have no known competing financial interests or personal relationships that could have appeared to influence the work reported in this paper.

Acknowledgments

The research work is a part of the activities of the Process and Energy Department in Delft University of Technology and the Johan Gadolin Process Chemistry Centre, a center of excellence financed by Åbo Akademi University. The authors acknowledge financial support from Åbo Akademi University, the Finnish Society of Science and Letters for Liangyuan Wei visiting the Laboratory of Industrial Chemistry and Reaction Engineering, Åbo Akademi University, Turku, Finland. The authors also acknowledge the PhD scholarship awarded to Liangyuan Wei by the China Scholarship Council (CSC). We thank Ruud Hendrikx and Wim Sloof at the Department of Materials Science and Engineering of the Delft University of Technology for the XRD and SEM analysis respectively. We thank Dr. Wiel H. Evers at the Department of Chemical Engineering of the Delft University of Technology for the TEM analysis.

Appendix A. Supplementary data

Supplementary material related to this article can be found, in the online version, at doi:https://doi.org/10.1016/j.apcata.2021.118012.

References

[1] A. Borgschulte, N. Gallandat, B. Probst, R. Suter, E. Callini, D. Ferri, Y. Arroyo, R. Erni, H. Geerlings, A. Züttel, Phys. Chem. Chem. Phys. 15 (2013) 9620–9625.
[2] S. Walspurger, G.D. Elzinga, J.W. Dijkstra, M. Sarić, W.G. Haije, Chem. Eng. J. 242 (2014) 379–386.
[3] C. Vogt, M. Monai, G.J. Kramer, B.M. Weckhuysen, Nat. Catal. 2 (2019) 188–197.
[4] R. Delmelle, R.B. Duarte, T. Franken, D. Burnat, L. Holzer, A. Borgschulte, A. Heel, Int J Hydrogen Energ 41 (2016) 20185–20191.
[5] L. Wei, H. Yang, B. Li, X. Wei, L. Chen, J. Shao, H. Chen, Int. J. Hydrogen Energy 39 (2014) 15416–15423.
[6] X.F. Yang, A.Q. Wang, B.T. Qiao, J. Li, J.Y. Liu, T. Zhang, Acc. Chem. Res. 46 (2013) 1740–1748.
[7] A. Wang, J. Li, T. Zhang, Nat. Rev. Chem. 2 (2018) 65–81.
[8] T. Yang, R. Fukuda, S. Hosokawa, T. Tanaka, S. Sakaki, M. Ehara, Chemcatchem 9 (2017) 1222–1229.
[9] S.X. Liang, C. Hao, Y.T. Shi, Chemcatchem 7 (2015) 2559–2567.
[10] Y.J. Chen, S.F. Ji, C. Chen, Q. Peng, D.S. Wang, Y.D. Li, Joule 2 (2018) 1242–1264.
[11] S.M.J. Rogge, A. Bavykina, J. Hajek, H. Garcia, A.I. Olivos-Suarez, A. Sepulveda-Escribano, A. Vimont, G. Clet, P. Bazin, F. Kapteijn, M. Daturi, E.V. Ramos-Fernandez, F.X.L.I. Xamena, V. Van Speybroeck, J. Gascon, Chem. Soc. Rev. 46 (2017) 3134–3184.
[12] L. Zhang, Y. Ren, W. Liu, A. Wang, T. Zhang, Sci. Rev. 5 (2018) 653–672.
[13] S. Abbet, A. Sanchez, U. Heiz, W.-D. Schneider, A.M. Ferrari, G. Pacchioni, N. Rösch, J. Am. Chem. Soc. 122 (2000) 3453–3457.
[14] H. Yan, H. Cheng, H. Yi, Y. Lin, T. Yao, C. Wang, J. Li, S. Wei, J. Lu, J. Am. Chem. Soc. 137 (2015) 10484–10487.
[15] A.W. Peters, Z. Li, O.K. Farha, J.T. Hupp, ACS Nano 9 (2015) 8484–8490.
[16] J. Zhang, X. Wu, W.-C. Cheong, W. Chen, R. Lin, J. Li, L. Zheng, W. Yan, L. Gu, C. Chen, Nat. Commun. 9 (2018) 1002.
[17] H.J. Qiu, Y. Ito, W. Cong, Y. Tan, P. Liu, A. Hirata, T. Fujita, Z. Tang, M. Chen, Angew. Chemie Int. Ed. English 54 (2015) 14031–14035.
[18] Y. Han, Y.-G. Wang, W. Chen, R. Xu, L. Zheng, J. Zhang, J. Luo, R.-A. Shen, Y. Zhu, W.-C. Cheong, C. Chen, Q. Peng, D. Wang, Y. Li, J. Am. Chem. Soc. 139 (2017) 17269–17272.
[19] P. Yin, T. Yao, Y. Wu, L. Zheng, Y. Lin, W. Liu, H. Ju, J. Zhu, X. Hong, Z. Deng, G. Zhou, S. Wei, Y. Li, Angew. Chemie Int. Ed. English 55 (2016) 10800–10805.
[20] Y. Chen, S. Ji, Y. Wang, J. Dong, W. Chen, Z. Li, R. Shen, L. Zheng, Z. Zhuang, D. Wang, Y. Li, Angew. Chemie Int. Ed. English 56 (2017) 6937–6941.
[21] Y. Qu, Z. Li, W. Chen, Y. Lin, T. Yuan, Z. Yang, C. Zhao, J. Wang, C. Zhao, X. Wang, F. Zhou, Z. Zhuang, Y. Wu, Y. Li, Nat. Catal. 1 (2018) 781–786.
[22] L. Chen, T. Horiuchi, T. Osaki, T. Mori, APPL CATAL B-ENVIRON 23 (1999) 259–269.
[23] C.A. Emeis, J. Catal. 141 (1993) 347–354.
[24] S. Abelló, C. Berrueco, D. Montané, Fuel 113 (2013) 598–609.
[25] S. Abate, K. Barbera, E. Giglio, F. Deorsola, S. Bensaid, S. Perathoner, R. Pirone, G. Centi, Ind. Eng. Chem. Res. 55 (2016) 8299–8308.
[26] D.J. Lensveld, J.G. Mesu, A.J. Van Dillen, K.P. de Jong, Microporous Mesoporous Mater. 44 (2001) 401–407.
[27] L. Wei, W. Haije, N. Kumar, J. Peltonen, M. Peurla, H. Grenman, W. de Jong, Catal. Today 362 (2021) 35–46.
[28] J.M. Newsam, Science 231 (1986) 1093–1099.
[29] J.G. Speight, Lange's Handbook of Chemistry, McGraw-Hill, New York, 2005.
[30] A. Luengnaruemitchai, A. Kaengsilalai, Chem. Eng. J. 144 (2008) 96–102.
[31] I. Graça, L.V. González, M.C. Bacariza, A. Fernandes, C. Henriques, J.M. Lopes, M. F. Ribeiro, Appl Catal B-Environ 147 (2014) 101–110.
[32] A. Laachir, V. Perrichon, A. Badri, J. Lamotte, E. Catherine, J.C. Lavalley, J. El Fallah, L. Hilaire, F. Le Normand, E. Quéméré, G. Noël Sauvion, O. Touret, J. Chem. Soc., Faraday Trans. 87 (1991) 1601–1609.
[33] K.O. Xavier, R. Sreekala, K.K.A. Rashid, K.K.M. Yusuff, B. Sen, Catal. Today 49 (1999) 17–21.
[34] P. Zimmer, A. Tschöpe, R. Birringer, J. Catal. 205 (2002) 339–345.
[35] W.X. Nie, X.J. Zou, X.F. Shang, X.G. Wang, W.Z. Ding, X.G. Lu, Fuel 202 (2017) 135–143.
[36] G. Socrates, Infrared and Raman Characteristic Group Frequencies: Tables and Charts, John Wiley & Sons, 2004.
[37] V.A. Suarez-Toriello, C.E. Santolalla-Vargas, J.A. de los Reyes, A. Vazquez-Zavala, M. Vrinat, C. Geantet, J Mol Catal A-Chem 404 (2015) 36–46.
[38] T.J. Strathmann, S.C.B. Myneni, Geochim Cosmochim Ac 68 (2004) 3441–3458.
[39] X. Ding, J. Ma, X. Zhou, X. Zhao, S. Hao, C. Deng, G. Li, J Sol-Gel Sci Techn 90 (2019) 296–304.
[40] Y.-F. Jiang, C.-Z. Yuan, X. Xie, X. Zhou, N. Jiang, X. Wang, M. Imran, A.-W. Xu, Acs Appl Mater Inter 9 (2017) 9756–9762.
[41] M. Lv, J. Zhou, Y. Zhang, Catal. Sci. Technol. (2019).
[42] Y. Wang, Z. Chen, P. Han, Y. Du, Z. Gu, X. Xu, G. Zheng, ACS Catal. 8 (2018) 7113–7119.
[43] H. Arandiyan, Y. Wang, J. Scott, S. Mesgari, H. Dai, R. Amal, Acs Appl Mater Inter 10 (2018) 16352–16357.

[44] W. Li, X. Nie, X. Jiang, A. Zhang, F. Ding, M. Liu, Z. Liu, X. Guo, C. Song, Appl Catal B-Environ 220 (2018) 397–408.
[45] F. Wang, S. He, H. Chen, B. Wang, L. Zheng, M. Wei, D.G. Evans, X. Duan, J. Am. Chem. Soc. 138 (2016) 6298–6305.
[46] J. Graciani, K. Mudiyanselage, F. Xu, A.E. Baber, J. Evans, S.D. Senanayake, D. J. Stacchiola, P. Liu, J. Hrbek, J.F. Sanz, J.A. Rodriguez, Science 345 (2014) 546–550.
[47] H.J.W. Lijun Wu, A.R. Moodenbaugh, R.F. Klie, Yimei Zhu, D.O. Welch, M. Suenaga, Phys. Rev. B 69 (125419) (2004) 125415.
[48] K. Yu, N. Kumar, A. Aho, J. Roine, I. Heinmaa, D.Y. Murzin, A. Ivaska, J. Catal. 335 (2016) 117–124.
[49] F. Benaliouche, Y. Boucheffa, P. Ayrault, S. Mignard, P. Magnoux, Microporous Mesoporous Mater. 111 (2008) 80–88.
[50] C. Wang, Q. Liu, J. Song, W. Li, P. Li, R. Xu, H. Ma, Z. Tian, Catal. Today 234 (2014) 153–160.
[51] Q. Pan, Jiaxi Peng, Tianjun Sun, Sheng Wang, Shudong Wang, Insight into the Reaction Route of CO2 Methanation: Promotion Effect of Medium Basic Sites, Catcom. 2013.10.034, 10, 2014, pp. 74–78.
[52] Y. Yan, Y.H. Dai, H. He, Y.B. Yu, Y.H. Yang, Appl Catal B-Environ 196 (2016) 108–116.
[53] L. Wei, N. Kumar, W. Haije, J. Peltonen, M. Peurla, H. Grénman, W. de Jong, Mol. Catal. 494 (2020), 111115.